Applied Physics Letters

Chipless wireless temperature sensor based on quasi-BIC resonance

Cite as: Appl. Phys. Lett. **119**, 193504 (2021); https://doi.org/10.1063/5.0064480
Submitted: 23 July 2021 • Accepted: 25 October 2021 • Published Online: 11 November 2021

Ildar Yusupov, Dmitry Filonov, Andrey Bogdanov, et al.

View Online Export Citation CrossMark

AIP Publishing

© 2021 Author(s).

Applied Physics Letters ARTICLE scitation.org/journal/apl

Chipless wireless temperature sensor based on quasi-BIC resonance

Cite as: Appl. Phys. Lett. **119**, 193504 (2021); doi: 10.1063/5.0064480
Submitted: 23 July 2021 · Accepted: 25 October 2021 ·
Published Online: 11 November 2021

View Online Export Citation CrossMark

Ildar Yusupov,[1,2,a)] Dmitry Filonov,[2,3] Andrey Bogdanov,[1,2] Pavel Ginzburg,[4] Mikhail V. Rybin,[1,5] and Alexey Slobozhanyuk[1,2,a)]

AFFILIATIONS

[1]School of Physics and Engineering, ITMO University, St. Petersburg 197101, Russia
[2]Sirius University of Science and Technology, 1 Olympic Ave., 354340 Sochi, Russia
[3]Center for Photonics and 2D Materials, Moscow Institute of Physics and Technology, Dolgoprudny 141700, Russia
[4]School of Electrical Engineering, Tel Aviv University, Tel Aviv 69978, Israel
[5]Ioffe Institute, Saint Petersburg 194021, Russia

[a)]Authors to whom correspondence should be addressed: ildar.yusupov@metalab.ifmo.ru and a.slobozhanyuk@metalab.ifmo.ru

ABSTRACT

Wireless sensors find use in many practical applications, where wired connections possess a limitation. New realms of global connectivity and data exchange among various devices suggest putting a sensor on a consumable level, where electronic circuits are not affordable from an economic standpoint. Chipless approaches, aiming to address the later issue, typically come with a penalty of performance degradation and, in many cases, is seen as a compromise solution. Here, we demonstrate a concept of the extremely sensitive temperature sensor based on the bound states in the continuum (BIC) approach. A ceramic half-cylinder above a ground plane is designed to support high quality factor supercavity modes with a strong resonant dependence on an ambient temperate. The operation of the sensor is experimentally demonstrated in a broad range of temperatures, spanning from 25 to 105 °C with an average sensitivity of 4 MHz/°C. The key element, leading to this performance, is high-quality ceramics, which allows supporting confined modes with moderately low Ohmic losses and extremely high-quality factors above 1000. High-performance chipless devices, which are capable to accommodate several functions with a single platform, open a venue to a new generation of wireless distributed sensors, where the main technological and outlay efforts are placed on an interrogation side.

Published under an exclusive license by AIP Publishing. https://doi.org/10.1063/5.0064480

Real-time wireless sensing is an essential capability to power modern systems, required to perform data collection, processing, and decision-making. The concept of the Internet of Things[1] for "Industry 4.0"[2] pushes wireless technologies to new frontiers, where high performance demands and severe cost limitations should find a compromise. Radio-frequency identification (RFID) is among the most promising technologies in this endeavor, as it puts the main outlay on an interrogator, while keeping an information holder (a tag) low cost. Passive RFID tags contain an antenna and a chip. The system rectifies a part of the incident energy and modulates a backscattered signal, sent by a reader. However, introducing an electronic circuitry elevates the tag's cost to several cents, which is unaffordable in many applications. Another aspect is an operation in harsh conditions, degrading performances of electronic components. High temperatures and chemically aggressive environments are among the representative examples. Chipless approaches come to address beforehand mentioned issues and are among new fast-growing trends in the field.[3] For example, chipless sensors were demonstrated to measure humidity,[4] pressure,[5] building integrity,[6] and many other important parameters.[7,8] Metamaterial-inspired sensors[9] and a sensor based on a microstrip patch antenna[10] were demonstrated for temperature measurements. Their operation principle is based on temperature-dependent materials' responses, leading to an averaged sensitivity of up to 0.05% frequency shift per degree.[11] However, monitoring foundries and jet turbines cannot be performed with an electronic circuitry, which is placed in a proximity to a heat source. Those applications demand using special material platforms. Dielectric resonators made of low-loss ceramic materials come at a rescue.[12,13]

One of the typical chipless sensor designs is based on a resonant shift, which occurs owing to a change in an environmental observable.[14] The accuracy depends on several factors, including electromagnetic properties of the resonator, dynamic ranges of measurement

Published under an exclusive license by AIP Publishing

apparatus, and signal-to-noise ratios in the wireless channel. We will put the last two factors apart and concentrate on the first system's parameter, as it is typically responsible for limitations in practical applications. As a rule of thumb, the accuracy depends on the quality factor (Q factor) of a resonator. The Q factor is bounded from above by material and radiation losses of the resonator. Those channels are the subject to a compromise. For example, wireless operation demands a mode leakage, which is linked to the radiation loss. The spectral shift, which is the key for the sensitivity, typically comes from a refractive index change in the resonator's material. However, changing the real part of the refractive index is accompanied by losses, according to Kramers–Kronig relations. Nevertheless, these limitations, typically faced in sensor designs, are not fundamental and can be bypassed with a proper choice of a material platform and a careful electromagnetic design.

Bound states in the continuum (BIC), being initially proposed as a mathematical concept in quantum mechanics almost a century ago, were generalized to many other fields, including classical electrodynamics. The essence of this general natural phenomenon is an interference between the high-Q confined mode and a continuum. Weak coupling between those two different families of modes leads to the emergence of high-Q resonances with far-field signatures (quasi-BIC or supercavity modes[15]). Those properties fit chipless sensor requirements for the best. Optical applications of quasi-BICs have been reviewed recently.[16] More specifically, metasurfaces supporting the quasi-BICs were investigated for ultra-thin layer measurements,[17] high-accuracy biosensing,[18] and optical refractometry.[19]

Here, we exploit supercavity modes in a single dielectric cylinder.[20,21] The structure is made of a high-quality high-index ceramic, which allows obtaining resonances with Q factors as high as 10^4 (Ref. 22) outperforming other architectures, e.g., Refs. 23 and 24. Those peculiar materials with designer-made permittivities, controllably ranging between 10 and 10 000 and with a loss tangent as small as 10^{-4} are the enabler for the experimental demonstration.

Figure 1 shows the layout of the proposed sensor that is a halved dielectric cylinder, placed on top of a metal ground plane. The structure is optimized to support a high-Q supercavity mode. Wireless

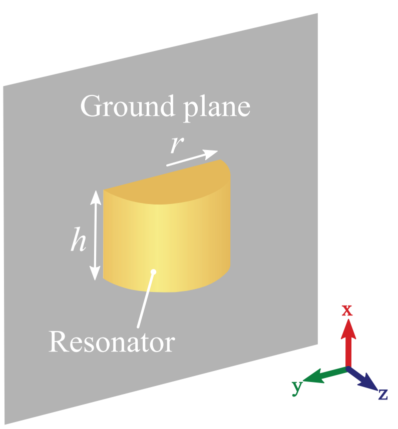

FIG. 1. Schematics of the temperature sensor. Halved dielectric cylinder attached to a ground plane. The resonator is probed with either a loop antenna or far-field interrogation with the polarization orthogonally to the axis of the cylinder.

sensing is performed with two different configurations, namely, a loop antenna or far-field interrogation. Reflection coefficients are measured by a vector network analyzer, and the spectral location of the resonance is retrieved. Being extremely high-Q, a supercavity mode is enormously sensitive to an ambient temperature, which affects the refraction index of the resonator. The spectral shift is then mapped on the temperature during the pre-calibration stage.

The supercavity modes emerge in a high-index dielectric resonator when two eigenmodes, associated with Mie and Fabry–Pérot resonances, undergo strong coupling that manifests itself as an avoided crossing pattern [Fig. 2(a) will be discussed hereafter]. Those states interfere destructively outside the resonator, realizing the quasi-BIC.[21] To find the supercavity mode condition, the parametrical study of the cylindrical dielectric resonator was performed using a frequency-domain solver of CST Microwave Studio. The dielectric resonator was excited by a loop antenna placed near the cylinder base, where the magnetic field maximum is expected. The complex reflection coefficient (S_{11}) was calculated numerically. The radius of the cylinder r was kept constant ($r = 15$ mm) while the height h was an optimization variable, modifying the aspect ratio r/h. Figure 2(a) summarizes the parametric studies. The color map shows (1-$|S_{11}|$) as a function of the cylinder's aspect ratio and operational frequency. Colored maxima on the graph correspond to the matching conditions between the probe and the modes within the structure.

The aspect ratio of 0.7 leads to the strong coupling of resonant cavity TE_{020} and TE_{012} modes and results in an emergence of the supercavity mode. TE means transverse electric, where the electrical field of the mode is primarily oriented orthogonally to the cylindrical resonator axis and sub-indices denote to the azimuthal, radial, and axial wavenumbers.[20] This parametric study allows finding optimal properties of the resonator $r = 15$ mm, $h = 21.42$ mm, permittivity $\varepsilon = 506$, and a loss tangent of 10^{-4}.

After identifying the parameters, consideration of a practical layout can be done. Our architecture consists of a halved dielectric cylinder, attached to a ground plane (Fig. 1). The metal sheet acts both as a holder and a heat source with moderately high heat conductivity. This approach also allows reducing the footprint of the device. From the electromagnetic standpoint, the ground plane acts as a mirror. In the case of a perfect electric conductor, the image theory suggests replicating responses of an entire geometry by considering its half. However, only modes with certain symmetries (granting the vanishing tangential component of the electrical field on the boundary) obey this rule. The modes, responsible to the quasi-BIC formation (TE_{020} and TE_{012}) satisfy the beforehand mentioned criterion, and, as a result, the entire geometry can be halved and placed above the ground plane. Starting from the parameters, found optimal for a solid cylinder, we made a minor optimization to adjust the device geometry in Fig. 1. The location of the probing loop with a radius of 5 mm was chosen at the point of the magnetic field maximum (obtained after the mode analysis). The loop is placed 1 mm apart from the resonator (Fig. 1). Figure 2(b) demonstrates reflection coefficient spectra ($|S_{11}|$) of a whole and half-cut cylinder (red and blue lines, respectively). Both spectra agree with each other with a minor shift of the resonance location, which is attributed to numerical aspects of the calculations. The electric field distribution of the supercavity mode is shown in the inset of Fig. 2(b). The mode consists of three polarization currents loops, where the flow in the central one is in the opposite direction with respect to the others.

Published under an exclusive license by AIP Publishing

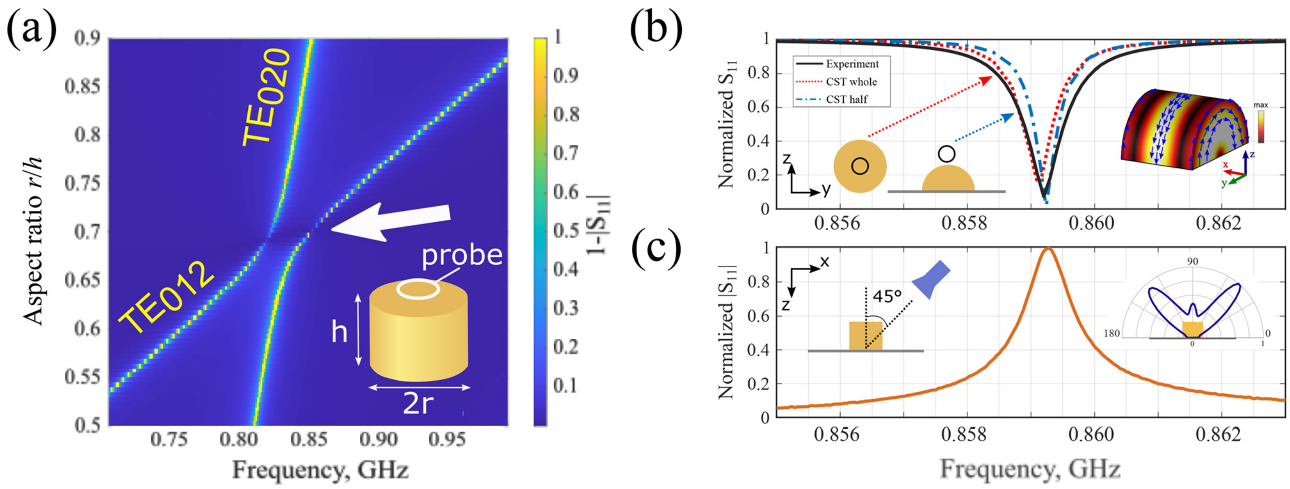

FIG. 2. (a) Numerically calculated color map of (1–$|S_{11}|$) as the frequency and aspect ratio *r*/*h*. S-parameters are obtained with the probe, as appears in the inset. (b) Numerically calculated and experimentally obtained reflection coefficient spectra ($|S_{11}|$) of the solid and halved dielectric resonators (curves clarifications appear in the legend). Inset shows numerically calculated electrical field intensity $|\mathbf{E}|$ of the quasi-BIC. Blue arrows depict the electric field polarization. (c) Experimentally obtained spectrum in the far-field configuration. Inset shows the measurement scheme and the normalized scattering diagram.

The high-Q state emerges owing to relatively low radiation efficiency and minor material losses despite the high modal confinement. Experimental response of the structure [black line, Fig. 2(b)] also verifies the existence of the high-Q mode. (The Q factor of the observed dip is 1070.)

While probing the structure response with the near-field coupled probe provides certain applied advantages, far-field interrogation is a benchmark of a wireless device. Here, we investigate the response in a monostatic scattering configuration. It should be noticed that the observation of high Q factors is directionally dependent. The inset in Fig. 2(c) shows the scattering diagram indicating that an optimal angle of 45° and 135° can be used for effective excitation of the high Q-modes.

The device is illuminated with the horn antenna at an angle of 45°, and the backscattering spectrum is obtained. The rectangular antenna is oriented along the Y-axis. Regardless the excitation configuration, the spectra in Figs. 2(b) and (c) demonstrate an excellent agreement in the strong response corresponding to the supercavity mode. After demonstrating the emergence of the quasi-BIC, sensing capabilities can be assessed. A gradual elevation in an ambient temperature leads to a change in the dielectric index, which shifts the resonant frequency of the supercavity mode. Since the aspect ratio remains constant, such a change in the dielectric index does not affect the condition for the excitation of the supercavity mode.[21] Thermal expansion in the range of the considered parameters can be neglected. Typically, an elevation of a material temperature is accompanied by increasing dielectric losses, leading to a drop in the resonance Q factor. However, it is quite remarkable that high-quality ceramics [here, we use (Ba,Sr)TiO_3[25]] are sustainable to elevated temperatures and maintain their electromagnetic properties quite well, as it will be shown hereafter.

Halved cylinder with radius $r = 15$ mm and height $h = 21.42$ mm, made of ceramic materials with permittivity $\varepsilon = 506$ and a loss tangent of 10^{-4}, was fabricated. The resonator is attached to a metallic ground plane (made of steel) with the dimensions of $30 \times 30\,\text{cm}^2$. The sensor can operate either with far-field excitation or with near-field loop antenna-based interrogation. The measurement in the far-field configuration is monostatic. The free-space normalized reflectance is demonstrated in Fig. 2(c) along with the measurement scheme shown in the inset. The horn antenna is pointed at a 45° angle to the resonator at a distance of 50 cm. We notice here that results collected in both near-field and far-field configurations match each other.

In the near-field setup, the resonator was excited by a small loop antenna connected to a vector network analyzer Rohde and Schwartz ZVB-40. The loop probe was calibrated and designed not to have a resonance at the range of frequencies between 0.85 and 1.25 GHz, where the experiment was performed. $|S_{11}|$ spectra have been measured. Figure 2(b) shows a comparison between numerically obtained and measured reflection coefficient spectra of the resonator at a room temperature of 21 °C. The experimental spectrum has a narrow resonance centered at $f_0 = 859.6$ MHz It is clearly seen that both numerical and experimental spectra are in a perfect agreement. Minor deviations or resonance positions come from an uncertainty in dielectric parameters of the cylinder, the finite size of the ground plane, and its material losses.

High-Q resonances are well approximated with a Lorentzian shape. Here, we fit the temperature-dependent peaks in (1- $|S_{11}|$) with this approach, evaluating the Q factor, resonance position f_0, and full width at half maximum (FWHM). For 21 °C, the Q factor of the supercavity mode was found to be Q = 1070, which is smaller than the predicted theoretical value (Q = 2000). However, it is still higher in comparison to the fundamental magnetic dipole mode with Q = 260. The high-Q supercavity resonance is sufficient for accurate temperature mapping. For this purpose, the sensor tag was heated with a hot air from a soldering station. The temperature of the ceramic resonator was monitored by a thermocouple connected to the multimeter. Figure 3(a) shows a set of resonant lines (1 – $|S_{11}|$) measured with the vector network analyzer. The corresponding ambient temperatures are

Published under an exclusive license by AIP Publishing

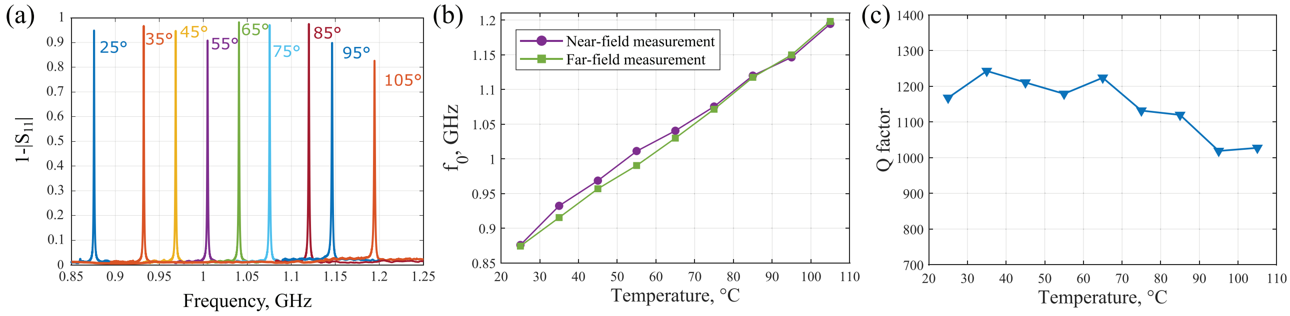

FIG. 3. The experimental demonstration of temperature sensing. (a) The measured reflection spectra ($1 - |S_{11}|$), demonstrating the resonance shift of the supercavity mode due to changes in the ambient temperature. (b) The measured resonance frequency in the case of near-field (purple curve) and far-field (green curve) measurements and (c) Q factor of peaks as a function of the temperature.

indicated in the plot. The sensor tag was examined at a temperature interval between 25 and 105 °C. Resonance frequencies f_0 vs temperature were extracted and are shown in Fig. 3(b) for both far-field and near-field measurements. As well as, Q factors were calculated and presented in Fig. 3(c) as a function of temperature. The resonance frequency shifts monotonically from 0.875 to 1.19 GHz with the temperature increase. Minor deviations from this behavior were observed and were attributed to non-uniform heating of the resonator. This problem was partially solved with a moderately low-rate temperature increase in the experiment.

An averaged absolute sensitivity (s) and a limit of detection (LOD) are essential characteristic parameters of any sensor.[26] In our case, the sensor's sensitivity is defined as $s = \Delta f_0/\Delta T = 4$ MHz/°C. The LOD is defined as a minimal detectable temperature change that can be estimated by the sensor and is given by LOD $= f_r/s$, where f_r is the resolution of the vector network analyzer $f_r = \Delta F/(n-1)$. Here, ΔF is the assessable frequency span, and n is a number of sampling points. In our case, $f_r = 0.06 \times 10^{-3}$ GHz, so LOD = 0.016 °C and can be further improved by reducing the observation range. It is worth noting that state-of-the-art vector network analyzers have frequency resolution as high as 0.1 Hz, leading to an enormously high predicted accuracy.[27] In this case, however, noise in the wireless channel will set a limitation. In any case, a small fraction of degree accuracy can be obtained with a second-scale observation time of the sensor. The figure of merit (FOM) defined as FOM $= s$/FWHM can serve as ultimate assessment criteria, as it is solely the function of sensitivity and linewidth of the resonance and does not depend on the measurement apparatus.[28] For our sensor, FOM = 5.

In summary, we have demonstrated an efficient temperature sensor based on quasi-BICs in the high-quality ceramic resonator. Our design is based on observing the high-Q supercavity mode in the geometry, consisting of the halved dielectric cylinder resonator, attached to a ground plane. A monotonic frequency shift of the resonant frequency with the ambient temperature increase from 25 to 105 °C has been observed for both far-field and near-field measurements. The device's sensitivity has been found to be as good as $\Delta f_0/\Delta T = 4$ MHz/°C. The demonstrated concept put low budget chipless sensors on the stage to compete with sophisticated devices on performances. As an outlook, ceramic resonators' platform, being recently demonstrated to show superior performances in RFID applications,[29,30] can be further toward the sensor fusion approach.

The reported study was funded by RFBR, Sirius University of Science and Technology, JSC Russian Railways and Educational Fund "Talent and success," project number 20-37-51011. A.S. acknowledges the support by the Foundation for the Advancement of Theoretical Physics and Mathematics "BASIS."

AUTHOR DECLARATIONS

Conflict of Interest

The authors have no conflicts to declare.

DATA AVAILABILITY

The data that support the findings of this study are available from the corresponding authors upon reasonable request.

REFERENCES

[1] L. D. Xu, W. He, and S. Li, IEEE Trans. Ind. Inf. **10**, 2233 (2014).
[2] H. Lasi, P. Fettke, H. G. Kemper, T. Feld, and M. Hoffmann, Bus. Inf. Syst. Eng. **6**, 239 (2014).
[3] V. Mulloni and M. Donelli, Sensors **20**, 2135 (2020).
[4] Y. Feng, L. Xie, Q. Chen, and L. R. Zheng, IEEE Sens. J. **15**, 3201 (2015).
[5] C. Schuster, P. Schumacher, M. Schusler, A. Jiménez-Sáez, and R. Jakoby, in Proceedings of IEEE Sensors (2017).
[6] S. Dey, R. Bhattacharyya, S. E. Sarma, and N. C. Karmakar, IEEE Internet Things J. **8**, 3955 (2021).
[7] C. Shi, A. Rani, B. Thomson, R. Debnath, A. Motayed, D. E. Ioannou, and Q. Li, Appl. Phys. Lett. **115**, 121602 (2019).
[8] Y. Li, Y. Yu, H. San, Y. Wang, and L. An, Appl. Phys. Lett. **103**, 013111 (2013).
[9] F. Lu, Q. Tan, Y. Ji, Q. Guo, Y. Guo, and J. Xiong, Sensors **18**, 2879 (2018).
[10] J. W. Sanders, J. Yao, and H. Huang, IEEE Sens. J. **15**, 5312 (2015).
[11] T. T. Thai, J. M. Mehdi, F. Chebila, H. Aubert, P. Pons, G. R. Dejean, M. M. Tentzeris, and R. Plana, IEEE Sens. J. **12**, 2756 (2012).
[12] H. Cheng, X. Ren, S. Ebadi, Y. Chen, L. An, and X. Gong, IEEE Sens. J. **15**, 1453 (2015).
[13] B. Kubina, M. Schusler, C. Mandel, A. Mehmood, and R. Jakoby, in *Proceedings of IEEE Sensors* (IEEE, 2013), p. 4.
[14] S. Dey, J. K. Saha, and N. C. Karmakar, IEEE Microwave Mag. **16**, 26 (2015).
[15] M. Rybin and Y. Kivshar, Nature **541**, 164 (2017).
[16] S. I. Azzam and A. V. Kildishev, Adv. Opt. Mater. **9**, 16 (2021).
[17] Y. K. Srivastava, R. T. Ako, M. Gupta, M. Bhaskaran, S. Sriram, and R. Singh, Appl. Phys. Lett. **115**, 151105 (2019).
[18] F. Yesilkoy, E. R. Arvelo, Y. Jahani, M. Liu, A. Tittl, V. Cevher, Y. Kivshar, and H. Altug, Nat. Photonics **13**, 390 (2019).
[19] D. N. Maksimov, V. S. Gerasimov, S. Romano, and S. P. Polyutov, Opt. Express **28**, 38907 (2020).

Published under an exclusive license by AIP Publishing

[20]A. A. Bogdanov, K. L. Koshelev, P. V. Kapitanova, M. V. Rybin, S. A. Gladyshev, Z. F. Sadrieva, K. B. Samusev, Y. S. Kivshar, and M. F. Limonov, Adv. Photonics **1**, 016001 (2019).
[21]M. V. Rybin, K. L. Koshelev, Z. F. Sadrieva, K. B. Samusev, A. A. Bogdanov, M. F. Limonov, and Y. S. Kivshar, Phys. Rev. Lett. **119**, 243901 (2017).
[22]M. Odit, K. Koshelev, S. Gladyshev, K. Ladutenko, Y. Kivshar, and A. Bogdanov, Adv. Mater. **33**, 2003804 (2021).
[23]D. Vovchuk, S. Kosulnikov, R. E. Noskov, and P. Ginzburg, Phys. Rev. B **102**, 094304 (2020).
[24]S. Kosulnikov, D. Filonov, A. Boag, and P. Ginzburg, Sci. Rep. **11**, 9571 (2021).
[25]E. A. Nenasheva, A. D. Kanareykin, N. F. Kartenko, A. I. Dedyk, and S. F. Karmanenko, J. Electroceram. **13**, 235 (2004).
[26]N. Pandit, R. K. Jaiswal, and N. P. Pathak, Electron. Lett. **56**, 985 (2020).
[27]M. Wendt, Report CERN-94-01, CAS—CERN Accelerator School: 5th General Accelerator Physics Course (2020).
[28]S. Romano, G. Zito, S. Torino, G. Calafiore, E. Penzo, G. Coppola, S. Cabrini, I. Rendina, and V. Mocella, Photonics Res. **6**, 726 (2018).
[29]D. Dobrykh, I. Yusupov, S. Krasikov, A. Mikhailovskaya, D. Shakirova, A. A. Bogdanov, A. Slobozhanyuk, D. Filonov, and P. Ginzburg, IEEE Trans. Antennas Propag. **69**, 3125 (2021).
[30]S. Krasikov, M. Odit, D. Dobrykh, I. Yusupov, A. Mikhailovskaya, D. Shakirova, A. Shcherbakov, A. Slobozhanyuk, P. Ginzburg, D. Filonov, and A. Bogdanov, Phys. Rev. Appl. **15**, 024052 (2021).

Published under an exclusive license by AIP Publishing